

# Vertical structure of biomass burning aerosol transported over the southeast Atlantic Ocean

Harshvardhan Harshvardhan<sup>1</sup>, Richard Ferrare<sup>2</sup>, Sharon Burton<sup>2</sup>, Johnathan Hair<sup>2</sup>, Chris Hostetler<sup>2</sup>, David Harper<sup>2</sup>, Anthony Cook<sup>2</sup>, Marta Fenn<sup>3</sup>, Amy Jo Scarino<sup>3</sup>, Eduard Chemyakin<sup>3</sup>, Detlef Müller<sup>4</sup>

<sup>1</sup>Purdue University, West Lafayette, IN, United States

<sup>2</sup>NASA Langley Research Center, Hampton, VA, United States

<sup>3</sup>Science Systems and Applications, Inc./NASA Langley Research Center, Hampton, VA, United States

<sup>4</sup>University of Hertfordshire, Hatfield, Hertfordshire, United Kingdom

*Correspondence to:* H. Harshvardhan (harshvar@purdue.edu)

**Abstract.** Biomass burning in southwestern Africa produces smoke plumes that are transported over the Atlantic Ocean and overlie vast regions of stratocumulus clouds. This aerosol layer contributes to direct and indirect radiative forcing of the atmosphere in this region, particularly during the months of August, September and October. There was a multi-year international campaign to study this aerosol and its interactions with clouds. Here we report on the evolution of aerosol distributions and properties as measured by the airborne high spectral resolution lidar (HSRL-2) during the ORACLES (Observations of Aerosols above Clouds and their intEractionS) campaign in September 2016. The NASA Langley HSRL-2 instrument was flown on the NASA ER-2 aircraft for several days in September 2016. Data were aggregated at two pairs of  $2^\circ \times 2^\circ$  grid boxes to examine the evolution of the vertical profile of aerosol properties during transport over the ocean. Results showed that the structure of the profile of aerosol extinction and microphysical properties is maintained over a one to two-day time scale. In the 3-5 km altitude range, 95% of the aerosol extinction was contributed by particles in the 0.05-0.50  $\mu\text{m}$  radius size range, with the aerosol in this size range having an average effective radius of 0.16  $\mu\text{m}$ . This indicates that there is essentially no scavenging or dry deposition at these altitudes. Moreover, there is very little day to day variation in these properties, such that time sampling as happens in such campaigns, may be representative of longer periods such as monthly means. Below 3 km there is considerable mixing with larger aerosol, most likely continental source near land. Furthermore, these measurements indicated that there was often a distinct gap between the bottom of the aerosol layer and cloud tops at the selected locations as evidenced by a layer of several hundred meters that contained relatively low aerosol extinction values above the clouds.

## 1 Introduction

Aerosols are often considered as the most confounding element in the climate system when simulating parameters of the Earth's current climate. Their interaction with clouds makes the problem extremely complicated. The general topic of aerosol-cloud interaction has been of great interest in the scientific community: to quote the report of the Intergovernmental Panel on Climate Change (IPCC AR5) "Clouds and aerosols continue to contribute the largest uncertainty to estimates and interpretations of the Earth's changing energy budget" (Boucher et al., 2013).

35 In the context of these interactions, the interplay of biomass burning (BB) aerosol and the stratocumulus clouds in  
36 the Southeast (SE) Atlantic is unique and crucial to the estimates of the energy budget of the region. This BB aerosol  
37 arises from the seasonal burning (July-October) of agricultural residue in the southwestern African Savannah and  
38 traverses large distances westward over the SE Atlantic Ocean. Unlike the aerosol from industrial activity and biofuels  
39 that intermingle with clouds in many regions (Ramanathan et al., 2001; Mechoso et al., 2013), these optically thick  
40 BB aerosol layers overlay vast stretches of marine stratus cloud in the SE Atlantic (Chand et al., 2009; Wilcox, 2010;  
41 Adebisi et al., 2015) where they have a direct radiative effect. The BB aerosol can also act as nuclei for cloud droplets  
42 and so cause a potentially significant cloud albedo effect. Observations and modelling studies of such interactions in  
43 the Southeast Atlantic and southern Africa regions include Diamond et al. (2018), Kacarab et al. (2020), Mallet et al.  
44 (2020) and Gupta et al. (2021). There is also some evidence that aerosol can alter the thermodynamics of cloud  
45 formation through semi-direct effects (Sakaeda et al., 2011). Studies using high resolution limited area models have  
46 shown a variety of effects, including stratus to cumulus transition resulting from these interactions (Yamaguchi et al.,  
47 2015; Gordon et al., 2018; Lu et al., 2018). The semi-direct effect has also been shown to be important in a limited  
48 time run of a global model (Das et al., 2020).

49 During the course of its transport over the Atlantic basin, the dense BB aerosol layer affects the underlying clouds  
50 and Earth's radiative balance in multiple ways. It exerts a direct radiative forcing (DRF) by scattering and absorbing  
51 solar radiation in the atmosphere; when clouds are present, these aerosols absorb incoming solar radiation along with  
52 the radiation reflected by the underlying cloud surface (Chand et al., 2009; Meyer et al., 2013; Zhang et al., 2016).  
53 Simultaneously, depending on the relative vertical location of the aerosol with respect to the cloud deck, the cloud  
54 cover (fraction) or liquid water path may increase or decrease in response to heating of surrounding air masses due to  
55 aerosol absorption and subsequent changes in atmospheric stability, the semi-direct forcing (Sakaeda et al., 2011;  
56 Wilcox, 2012; Das et al., 2020). Observations at Ascension Island show that daytime cloud cover and relative humidity  
57 are lower when there is more smoke in the marine boundary layer (Zhang and Zuidema, 2019). Moreover, as the  
58 marine boundary layer (MBL) deepens farther offshore and north of 5°S, subsiding aerosol particles become entrained  
59 into the MBL and interact with the clouds as cloud condensation nuclei to affect their microphysics (indirect forcing)  
60 (Costantino and Breon, 2013; Painemal et al., 2014).

61 In the context of simulating the above alluded aerosol radiative effects, it is vital that aerosol-cloud overlap  
62 characteristics are accurately represented within the models. The quantification of these aerosol-cloud overlap  
63 characteristics in the models is necessary for a variety of reasons. For example, previous studies have found that the  
64 sign and magnitude of DRF of absorbing aerosol above clouds (AAC) critically depends upon the reflectance and  
65 coverage of the underlying cloud surfaces along with the optical properties, composition and size distribution of the  
66 overlying aerosols (Keil and Haywood, 2003; Chand et al., 2009). Additionally, the magnitude and sign of the aerosol  
67 semi-direct effects are quite sensitive to the vertical distribution of aerosols, especially with respect to the vertical  
68 location of clouds (Penner et al., 2003; McFarquhar and Wang, 2006; Koch and Del Genio, 2010).

69 Here we address the evolution of the vertical properties of BB aerosol as it travels in the marine environment after  
70 leaving the African land mass. Section 2 identifies the field campaign and specifies the geographic region selected for  
71 the analysis and rationale for that choice. Section 3 describes the attributes of the instrument and key parameters

72 related to the aerosol that can be extracted from the measurements. Section 4 presents the results followed by a  
73 summary and conclusion in section 5.

## 74 **2 Field Campaigns**

75 The concerns mentioned above were the driving force behind plans for several international multi-year field  
76 campaigns; ORACLES (Observations of Aerosols above Clouds and their intEractionS, Redemann et al., 2021),  
77 CLARIFY-2017 (CLoud-Aerosol-Radiation Interactions and Forcing for Year 2017, Haywood et al., 2021), and  
78 LASIC (Layered Atlantic Smoke Interactions with Clouds, Zuidema et al., 2016, 2018). A key component of the  
79 September 2016 NASA ORACLES Intensive Observation Period (IOP) was the vertical profiling of aerosol properties  
80 measured by an airborne lidar, the NASA Langley High Spectral Resolution Lidar-2, HSRL-2 (Burton et al., 2018),  
81 on-board the NASA ER-2, which was based in Walvis Bay, Namibia, for operations during 2016, the deployment  
82 covered in this study. In the following two years, the instrument was on-board the P-3 flying out of São Tomé. The  
83 siting and flight tracks chosen ensured adequate coverage of the seasonal BB aerosol.

### 84 **2.1 Meteorology**

85 The September monthly mean meteorological situation is shown in Fig. 1 from MERRA2 reanalysis (Buchard et  
86 al., 2017; Randles et al., 2017) along with locations of relevant sites. A thorough meteorological analysis for all  
87 ORACLES deployments is provided in Ryoo et al. (2021). For the period under consideration here, they found that  
88 the African Easterly Jet-South (AEJ-S), fast moving zonal easterlies centered on 650 hPa around 5-15°S, was active  
89 and corresponded closely to the long-term climatology. Fig. 2 shows 650 hPa winds from MERRA2 reanalysis at the  
90 beginning, at the end, and on two intermediate days during which HSRL-2 measurements were made. ER-2 flight  
91 tracks during the September 2016 IOP are shown in Fig. 3. Note that flights were primarily confined to within roughly  
92 1000 km of the African coast with only the 22 September flight venturing further. Flights such as executed during the  
93 IOP are unable to follow air parcels in a Lagrangian fashion to examine the evolution of smoke plumes. Here we  
94 provide an alternate framework by which to study evolving aerosol properties in an average sense. In order to establish  
95 average characteristics of the BB smoke plume as it travels over the ocean, we have chosen five grid boxes of two-  
96 degree latitude and longitude on a side at various distances from the source and aggregated observations. The choice  
97 of grid boxes was based on the availability of data from the flights (Fig. 3) and the general direction of transport of  
98 the smoke as evidenced by the wind fields in Fig. 2. The grid boxes so chosen are marked on Figs. 2 and 3 and the  
99 rationale for the choice is explained below.

100 Figure 4 shows 48-hour backward trajectory frequency analyses at 3.5 km, roughly the central altitude of the plume,  
101 using NOAA HYSPLIT trajectory calculations ([https://www.ready.noaa.gov/HYSPLIT\\_traj.php](https://www.ready.noaa.gov/HYSPLIT_traj.php)) which were carried  
102 out using archived GDAS 0.5-degree meteorology (Stein et al., 2015). The frequency distribution is a 48-hour history  
103 of the paths taken by air parcels arriving at the grid boxes marked A and C at 3500 m altitude. The time period of the  
104 frequency analyses covers the entire period during which HSRL-2 measurements were made, 12-24 September 2016.

105 The selected grid box pairs indicate that Box A receives aerosol that has earlier crossed Box B and Box C is downwind  
106 of Box D; boxes B and D receive aerosol directly from BB sources on land. The grid box pairs A/B and C/D can  
107 therefore provide information on the evolution of the microphysics and vertical distribution of BB aerosol plumes  
108 after leaving the continent. This strategy is similar to that used in comparisons of models with observations for this  
109 campaign by Shinozuka et al. (2020), who also showed that observations made on the sampled days were  
110 representative of monthly means. In addition to the four boxes strongly influenced by smoke, a southern box, E, has  
111 been chosen to provide a control contrast to the other areas in that it is influenced primarily by maritime air as seen  
112 from Figs. 1 and 2.

## 113 **2.2 ORACLES 2016 IOP**

114 The days during the campaign that were included in the averaging procedure are shown in Table 1. Also included  
115 is the typical time of the day when the measurements were made, a function of the flight pattern of the ER-2. The  
116 number of lidar return profiles averaged for each grid box and statistics related to the backward trajectories are also  
117 listed. These grid boxes contained aircraft tracks on multiple days during which trajectory analysis showed near-  
118 uniform wind direction between 2.5 and 4.5 km altitude throughout the IOP. With the exception of the grid box  
119 centered at 22° S, 9° E, all indicate flow from the source region of BB aerosol. Table 1 also lists the mean and standard  
120 deviation of time duration in hours spent over water of air parcels arriving at 3500 m altitude at the grid box during  
121 the averaging period. There is no entry for Box E since arriving air had a maritime source and did not originate from  
122 land. It must be stressed that the duration is not calculated from the source region on land, which is distributed over a  
123 large area of central Africa (e.g., Fig. 9 of Redemann et al., 2021) and cannot be uniquely identified with specific  
124 observations made over the ocean. The plume has already been airborne over land for several hours (see Fig. 4) and  
125 aerosol would have undergone transformations that occur at short time scales (Cappa et al., 2020). The duration was  
126 calculated by running HYSPLIT backward trajectories of air parcels arriving every six hours starting at 0600 UTC on  
127 the days of the first flight and ending at 1800 UTC on the days of the last flight of the averaging period and is shown  
128 in some detail in Fig. 5, which essentially reflects the profile of the prevailing wind speeds. The inference is that BB  
129 smoke at 3500 m altitude arrives at A on average about 30 h after passing B and arrives at C 35 h after passing D. The  
130 change in selected aerosol properties as measured by the HSRL-2 during this travel in the marine environment provides  
131 information on the evolution of the plume during this time period.

## 132 **3 HSRL-2**

133 The NASA LaRC HSRL-2 uses the HSRL technique to independently retrieve aerosol extinction and backscatter  
134 (Shipley et al., 1983; Grund and Eloranta, 1991; She et al., 1992) without a priori assumptions on aerosol type or  
135 extinction-to-backscatter ratio. By using the HSRL technique, HSRL-2, like its predecessor HSRL-1 (Hair et al.,  
136 2008), provides accurate backscatter profiles even in situations where the lidar beam is attenuated by overlying cloud  
137 or aerosol as long as it is not completely attenuated. The LaRC HSRL-2 employs the HSRL technique at 355 and 532

138 nm and the standard backscatter technique at 1064 nm. It also measures aerosol and cloud depolarization at all three  
139 wavelengths. The HSRL-2 provides vertically resolved measurements of the following extensive and intensive aerosol  
140 parameters below the aircraft (approximate archival horizontal,  $\Delta x$ , and vertical resolutions,  $\Delta z$ , are listed assuming  
141 ER-2 cruise speed).

142 • *Extensive parameters*<sup>1</sup> – backscatter coefficient,  $\beta$ , at 355, 532 and 1064 nm ( $\Delta x \sim 2$  km,  $\Delta z \sim 15$  m); extinction  
143 coefficient,  $\alpha$ , at 355, and 532 nm ( $\Delta x \sim 12$  km,  $\Delta z \sim 300$  m); optical depth at 355 and 532 nm (integrating the profile  
144 of extinction). The aerosol optical depth (AOD) is a critical quantity in discussions of the influence of aerosol on  
145 climate (Boucher et al., 2013).

146 • *Intensive parameters* – extinction-to-backscatter ratio of aerosol, the Lidar Ratio,  $S_a = \alpha_a / \beta_a$ , at 355 and 532 nm  
147 ( $\Delta x \sim 12$  km,  $\Delta z \sim 300$  m); depolarization,  $\delta_a = \beta_a^+ / \beta_a^{\parallel}$ , at 355, 532, and 1064 nm ( $\Delta x \sim 2$  km,  $\Delta z \sim 15$  m); and  
148 aerosol backscatter wavelength dependence (i.e., Ångström exponent for aerosol backscatter – directly related to the  
149 backscatter color ratio) for two wavelength pairs (355-532 and 532-1064 nm,  $\Delta x \sim 2$  km,  $\Delta z \sim 15$  m).

150 The overall systematic error associated with the backscatter calibration is estimated to be less than 5 % for the 355  
151 and 532 nm channels and 20 % for 1064 nm (Burton et al., 2015). Under typical conditions, the total systematic error  
152 for extinction is estimated to be less than  $0.01 \text{ km}^{-1}$  at 532 nm. The random errors for all aerosol products are typically  
153 less than 10 % for the backscatter and depolarization ratios (Hair et al., 2008). Rogers et al. (2009) validated the HSRL  
154 extinction coefficient profiles and found that the HSRL extinction profiles are within the typical state-of-the-art  
155 systematic error at visible wavelengths (Schmid et al., 2006). Since HSRL-2 includes the capability to measure  
156 backscatter at three wavelengths and extinction at two wavelengths, “ $3\beta+2\alpha$ ” microphysical retrieval algorithms  
157 (Müller et al., 1999a, 1999b; Veselovskii et al., 2002) are used to retrieve height-resolved parameters such as aerosol  
158 effective radius and number, surface and volume concentrations (Müller et al., 2014, Sawamura et al., 2016). Here we  
159 restrict ourselves to the effective radius of the particles.

## 160 **4 Results**

161 In this study of the vertically resolved evolving properties of BB aerosol, we present key lidar measurements and  
162 microphysical results obtained by performing the “ $3\beta+2\alpha$ ” retrieval mentioned in Section 3.

163

164

---

<sup>1</sup> By the term *extensive*, we refer to optical parameters, such as extinction, that are influenced by the amount (concentration) and type (size, composition, shape) of aerosol/cloud particles. *Intensive* properties, on the other hand, are those that depend only on the nature of the particles and not on their quantity or concentration, but rather depend only on aerosol type (Anderson et al., 2003).

## 165 4.1 Lidar

166 Vertical profiles averaged over the times of overflight in  $2^\circ \times 2^\circ$  latitude/longitude boxes shown in Figure 3 on the  
167 days given in Table 1 are for the following properties.

- 168 1. Aerosol Extinction at 532 nm,  $\alpha_a$ , determined by aerosol number concentration, microphysical  
169 properties and relative humidity
- 170 2. Backscatter Ångström exponent between 1064 and 532 nm, an indication of particle size.
- 171 3. Aerosol Depolarization at 532 nm, a measure of particle asphericity.
- 172 4. Aerosol extinction to backscatter ratio, the Lidar Ratio, at 532 nm, a marker for aerosol composition.

173 Inspection of the wind field at 650 hPa in Fig. 2 and backward trajectory frequency plots in Fig. 4 suggest that the  
174 grid boxes chosen fit naturally into two pairs of tracks of the widespread BB aerosol field. The northern pair, identified  
175 in Table 1 as A and B, centered around  $10^\circ$  S, are in a faster zonal track, whereas the grid boxes C and D are in a track  
176 centered between  $13\text{-}15^\circ$  S that is slightly slower and has a component from the north over a stretch of water (Fig. 2).  
177 The two pairs can then provide information on the evolution of aerosol properties over a time scale of one to two days.  
178 Figures 6-9 show the aerosol extinction, backscatter Ångström exponent, aerosol depolarization and Lidar Ratio for  
179 the two pairs of grid boxes and Box E, which is at the southern edge of the region influenced by the BB aerosol. The  
180 results presented are one-minute averages of independent 10 s vertical profiles for backscatter Ångström exponent  
181 and depolarization and one-minute averages for extinction and lidar ratio profiles. From Table 1, the mean time elapsed  
182 between B and A is 29.4 h and that between D and C is 34.9 h. It should be pointed out that parameter values shown  
183 below the level of mean cloud top are averages of lidar returns through breaks in the stratus deck and are not relevant  
184 for this study. If we use the low cut-off of an extinction coefficient of  $15 \text{ Mm}^{-1}$  to indicate an aerosol-free layer  
185 (Shinozuka et al., 2020), then Fig. 6 indicates that the bulk of the smoke layers encountered at these distances from  
186 land were separated from the cloud top, a feature more prevalent during the 2016 IOP than in 2017 and 2018  
187 (Redemann et al., 2021).

188 The northern plume is a column of aerosol of relatively constant extinction from just above 2.5 km to 5 km while  
189 the southern plume has a profile of extinction that increases nearly linearly with height from a minimum near the cloud  
190 top to a maximum at 5 km (Fig. 6). The vertical structure of the aerosol profiles measured by HSRL-2 was compared  
191 to water vapor profiles represented by the Modern-Era Retrospective analysis for Research and Applications, Version  
192 2 (MERRA2) model. Pistone et al. (2021) explored the relationship between aerosols, CO, water vapor as measured  
193 by ORACLES airborne in situ measurements and represented by models including MERRA2. They found the  
194 MERRA2 water vapor profiles, like the measured water vapor profiles, exhibited a linear relationship with CO and  
195 biomass burning plume strength; they also found that smoky, humid air produced by daytime convection over the  
196 continent advected over the ocean and into the ORACLES study region. MERRA2 water vapor profiles produced at  
197 three hourly increments and 72 pressure levels were interpolated to the times and locations of the HSRL-2 profiles.  
198 Water vapor mixing ratio generally decreased significantly just above the PBL then increased for altitudes around 2  
199 to 3 km before decreasing again. This behavior is generally consistent with the relationship between water vapor and  
200 aerosol scattering reported by Pistone et al. (2021).

201 Figure 10 shows the median, 25<sup>th</sup> and 75<sup>th</sup> percentile relative humidity (RH) profiles computed by interpolating the  
202 MERRA2 0.5-deg. 3-hourly humidity profiles to the locations and times of the HSRL-2 measurements. The profiles  
203 typically show a more pronounced increase in RH with altitude that more closely follows the HSRL-2 measurements  
204 of aerosol extinction profiles, although the MERRA2 profiles typically begin decreasing above 4 km whereas the  
205 airborne in situ RH measurements and HSRL-2 aerosol extinction profiles begin decreasing above 5 km. Interestingly,  
206 during three of the dates (Sept. 12, 16, 22) considerable portions of the smoke layers correspond to MERRA2 relative  
207 humidity above 60-70%. This increase in RH with altitude could help explain at least some of the increase in aerosol  
208 extinction with height observed in the HSRL-2 profiles of the C/D Box pair. Aerosol humidification often amplified  
209 the increase in aerosol extinction by factors of 1.5 or more (Doherty et al., 2022).

210 The Ångström exponent (Fig. 7) and depolarization (Fig. 8) indicate the presence of fine spherical particles at the  
211 top of the plume and increasing sizes towards the bottom. The Lidar Ratio (Fig. 9) above 3 km for the two pairs is  
212 between 70 and 80 sr, suggesting strong absorption (Müller et al., 2019) but is considerably less and highly variable  
213 in Box E and in the lower layers of the aerosol plume in Box D, where the smoke plume most likely has components  
214 of continental aerosol such as dust and pollution typical of the nearby Namibian coast (Klopper et al., 2020). The most  
215 striking feature of the results is the very small profile-to-profile variability of the intensive lidar parameters in the  
216 upper two kilometers of the plume over the course of several days as evident from the range of values in the 25-75  
217 percentile shaded grey in Figs. 7-9. This suggests strongly that the particles maintain their size, shape and absorbing  
218 properties over the first few days of transport over the ocean. This result is of some importance for climate studies in  
219 which the radiative properties of BB aerosol are input to the calculation of radiative forcing. Complex chain aggregates  
220 as found near the source of fires (Pósfai et al., 2003, China et al., 2013) are typically not represented in climate models.  
221 However, if the aerosol is already spherical and maintains its size over the time period of radiative interactions being  
222 studied, then core-shell models of varying degrees of complexity could perhaps suffice (Zhang et al., 2020). The lower  
223 portion of the plume containing larger BB aerosol particles is subject to mixing with marine and continental particles  
224 from regions not affected by biomass burning and is highly variable in nature. This would be more difficult to model  
225 but Fig. 6 shows that the aerosol extinction coefficient decreases rapidly at lower levels so errors in representation  
226 may be acceptable.

## 227 4.2 Microphysics

228 The lidar measurements are inverted to obtain information regarding particle size. The inversion is performed on one-  
229 minute averages of six independent 10 s backscatter profiles and one-minute average extinction profiles. Details of  
230 the inversion process are in Müller et al. (2019) and references therein. The particle size distribution is represented  
231 using a series of eight triangular basis functions that can represent both monomodal and bimodal size distributions  
232 (*ibid*). Points to note are that the procedure makes the following assumptions: the particles are spherical and  
233 homogeneous having wavelength-independent complex index of refraction. The low (< 5 %) values of depolarization  
234 through most of the plume, shown in Fig. 8, suggests that the spherical assumption is justified. There is most likely  
235 structure and inhomogeneity in the core of the particles, but current particle optical models are unable to incorporate

236 these complexities. Results from this inversion procedure have been compared to coincident airborne in situ particle  
237 measurements. Müller et al. (2014) present results from a campaign off the northeast coast of the US showing that the  
238 inversion results agree with in situ measurements of effective radius and also number, surface area and volume  
239 concentration within error bars. Sawamura et al. (2017) report on campaigns in the wintertime San Joaquin Valley of  
240 California and summertime near Houston, TX. They found high correlation and low bias in surface and volume  
241 concentration in situ measurements relative to HSRL with the best agreement for submicron fine-mode aerosol, which  
242 is most relevant to the current study. Müller et al. (2019) report retrievals and their uncertainty for one day in the  
243 ORACLES campaign, 22 September 2016. Considering only optical data with strong signal-to-noise ratio, they  
244 estimate retrieval errors are 25 % for number concentration. The relative uncertainty in effective radius for parts of  
245 the flight track where particle size was nearly constant was below 20 %.

246 In order to help separate particles that have BB source from coarser particles of continental or marine origin, we  
247 specify a Submicron Fraction (SMF) as the contribution to the extinction at 532 nm of particles in the radius range  
248 0.05-0.50  $\mu\text{m}$  (Anderson et al., 2005). Figure 11 shows the profiles of SMF for the five grid boxes and not surprisingly,  
249 the bulk of the smoke plume, especially between 3 and 5 km contains aerosol almost entirely in the submicron range.  
250 Below 3 km, at locations both near and further way from the coast, there is a marked increase in the fraction of larger  
251 particles. The increase in depolarization (Fig. 8) at these lower levels and a decrease in the Lidar Ratio (Fig. 9) suggest  
252 mixing with the aforementioned non-BB aerosol particles. However, the sharp decrease in extinction below 3 km (Fig.  
253 6) indicates that their contribution to direct radiative effects would be minimal. Finally, Fig. 12 shows the vertical  
254 profile of the effective radius of the SMF aerosol population. The effective radius is 0.16  $\mu\text{m}$  with little variation  
255 between 3 and 5 km. Of greater significance is that it remains very similar between the pairs of grid boxes along the  
256 transport trajectory of the smoke. The retrieved effective radius is similar to the results presented by Müller et al.  
257 (2014) for a mixture of urban aerosol and smoke. Their comparison with in situ measurements showed a slight  
258 overestimate but within a standard deviation. The retrieved and in situ results also show that the particle size is uniform  
259 with altitude even when the number concentration drops by a factor of three. Another set of prior comparisons of  
260 HSRL-2 and in situ measurements is provided in Sawamura et al. (2017). Here again, the effective radius of the  
261 submicron fraction of particles, 0.15  $\mu\text{m}$ , is uniform with altitude, and comparable though biased slightly low  
262 compared to in situ observations.

263 The effective radii of the SMF aerosols, which typically vary between 0.15 to 0.20  $\mu\text{m}$ , are generally consistent  
264 with the sizes reported previously for smoke aerosol in the ORACLES region. Haywood et al. (2021) provide a  
265 composite of the aerosol sizes for biomass burning aerosol off the South African coast. These size distributions, which  
266 were derived from airborne in situ measurements (Haywood et al., 2003; Peers et al., 2019; Wu et al., 2020), typically  
267 correspond to SMF aerosol effective radii between 0.14-0.17  $\mu\text{m}$  and were for the dry aerosol. As discussed in section  
268 4.1, the RH on some days was above 60-70% so that effective radii under ambient conditions could be expected to be  
269 somewhat higher than for the dry aerosol. Using measurements from an airborne Differential Aerosol Sizing and  
270 Hygroscopicity Spectrometer Probe (DASH-SP), Shingler et al. (2016) quantified the size-resolved growth factors for  
271 several aerosol types; they found that at RH~70-80%, particle diameters for biomass burning aerosols were about 15-  
272 20% larger than for the dry aerosol. Xu et al. (2021) derived aerosol properties during the 2016 ORACLES mission



273 using an inversion algorithm that combined HSRL-2 and Research Scanning Polarimeter (RSP) remote sensing  
274 measurements. These retrieved aerosol properties were then compared with those derived from airborne in situ  
275 measurements. For measurements acquired on Sept. 12, 2016, the SMF aerosol effective radius derived from the  
276 remote sensing measurements were generally between 0.12-0.15  $\mu\text{m}$  and were only slightly (0.012  $\mu\text{m}$ ) higher than  
277 the effective radii for the (dry) SMF aerosol derived from the airborne in situ size distribution measurements. This  
278 suggests that some of this difference is associated with differences in RH between the remote sensing retrievals and  
279 the in situ measurements.

## 280 **5 Conclusions**

281 The results of the aggregated HSRL-2 profiles during the 2016 ORACLES IOP presented here show two main  
282 findings. These are however limited to a brief period in the transport of BB smoke from continental Africa over marine  
283 clouds in the Atlantic Ocean. This is a limitation of the 2016 campaign because the flight tracks remained within 1000  
284 km of the coast. For the period of one to two days after crossing the land-ocean boundary, the fraction of all particles  
285 that are in the submicron range in the main smoke plume between 3 and 5 km is around 95 %. The effective radius of  
286 the submicron particles in this altitude interval is 0.16  $\mu\text{m}$  and essentially constant with altitude. The particle size is  
287 comparable to measured particle sizes in previous campaigns that sampled aerosol that was a mixture of urban haze  
288 and smoke (Müller et al., 2014; Sawamura et al., 2017). Moreover, the shape of the median vertical profile of  
289 extinction does not change during the first two days of transport over water suggesting the absence of dry deposition  
290 and wet scavenging. The low ( $< 0.05$ ) depolarization ratio of the submicron particles signifies that they are well coated  
291 and the assumption of sphericity in the inversion procedure and models that estimate the radiative effects of aerosol  
292 is justified. The BB aerosol mix with continental and marine aerosol at the base of the plume but during the September  
293 2016 IOP this layer of mixed aerosol tended to have very low extinction coefficients suggesting low abundance and  
294 there was often a distinct gap between the plume and the cloud tops.

295 The HSRL-2 instrument was also deployed in the 2017 and 2018 ORACLES campaigns but was deployed on the  
296 NASA P-3 which often flew at low altitude to acquire in situ measurements of aerosols and clouds. Consequently, the  
297 HSRL-2 was not able to make continuous measurements of the BB aerosol plumes in a manner similar as when  
298 deployed on the ER-2. However, there are segments of the track that can provide similar information to the data  
299 obtained in the 2016 campaign but for a different time period. Moreover, some flight tracks extended much further  
300 from land (Doherty et al., 2021). Analysis of the later campaigns will provide information on the physical evolution  
301 of aerosol that has aged for a longer period than is covered in this study.

## 302 **Data Management**

303 HSRL-2 optical data and retrieved inversion data are available at the NASA archive site  
304 <https://espoarchive.nasa.gov/archive/browse/oracles/id8/ER2> and are permanently archived at  
305 doi:10.5067/SUBORBITAL/ORACLES/ER2/2016\_V1.

306 **Acknowledgements**

307 The lead author would like to thank NASA Langley Research Center for hosting him during a sabbatical when this  
308 study was initiated. HSRL-2 participation in ORACLES was supported by NASA through the Earth Venture  
309 Suborbital-2 (EVS-2) program (grant no. 13-EVS2-13-0028). Funding for this work was also provided by NASA  
310 through the Radiation Sciences Program. We wish to thank the NASA ER-2 pilots and ground crew for their extensive  
311 support during ORACLES.

312

- 314 Anderson, T. L., Charlson, R. J., Winker, D. M., Ogren, J. A., and Holmén, K.: Mesoscale variations of tropospheric  
315 aerosols, *J. Atmos. Sci.*, 60(1), 119-136, 2003.
- 316 Anderson, T. L., Wu, Y., Chu, D. A., Schmid, B., Redemann, J., and Dubovik, O.: Testing the MODIS satellite  
317 retrieval of aerosol fine-mode fraction, *J. Geophys. Res.*, 110, D18204, doi:10.1029/2005JD005978, 2005.
- 318 Adebisi, A. A., Zuidema, P., Chang, I., Burton, S. P., and Cairns, B.: Mid-level clouds are frequent above the Southeast  
319 Atlantic stratocumulus clouds, *Atmos. Chem. Phys.*, 20, 11025-11043, doi:10.5194/acp-20-11025-2020, 2020.
- 320 Boucher, O., Randall, D., Artaxo, P., Bretherton, C., Feingold, G., Forster, P., Kerminen, V.-M., Kondo, Y., Liao, H.,  
321 Lohmann, U., Rasch, P., Satheesh, S. K., Sherwood, S., Stevens, B., and Zhang X.Y.: Clouds and Aerosols. In:  
322 *Climate Change 2013: The Physical Science Basis. Contribution of Working Group I to the Fifth Assessment Report*  
323 *of the Intergovernmental Panel on Climate Change [Stocker, T. F., Qin, D., Plattner, G.-K., Tignor, M., Allen, S.*  
324 *K., Boschung, J., Nauels, A., Xia, Y., Bex V., and Midgley, P. M. (eds.)]. Cambridge University Press, 2013.*
- 325 Buchard, V., Randles, C. A., da Silva, A. M., Darmenov, A., Colarco, P. R., Govindaraju, R., Ferrare, R. A., Hair, J.,  
326 Beyersdorf, A. J., Ziemba L. D., and Yu, H.: The MERRA-2 aerosol reanalysis, 1980 onwards Part II: Evaluation  
327 and case studies, *J. Climate*, 30, 6851-6871, doi:10.1175/JCLI-D-16-0613.1, 2017.
- 328 Burton, S. P., Hostetler, C. A., Cook, A. L., Hair, J. W., Seaman, S., Scola, S., Harper, D. B., Smith, J. A., Fenn, M  
329 A., Ferrare, R. A., Saide, P. E., Chemyakin, E. V., and Müller, D.: Calibration of a high spectral resolution lidar  
330 using a Michelson interferometer with data examples from ORACLES, *Appl. Optics*, 57, 6061-6075, 2018.
- 331 Burton, S. P., Hair, J. W., Kahnert, M., Ferrare, R. A., Hostetler, C. A., Cook, A. L., Harper, D. B., Berkoff, T. A.,  
332 Seaman, S. T., Collins, J. E., Fenn, M. A., and Rogers, R. R.: Observations of the spectral dependence of linear  
333 particle depolarization ratio of aerosols using NASA Langley airborne High Spectral Resolution Lidar, *Atmos.*  
334 *Chem. Phys.*, 15, 13453–13473, doi.org/10.5194/acp-15-13453-2015, 2015.
- 335 Cappa, C. D., Lim, C. Y., Hagan, D. H., Coggon, M., Koss, A., Sekimoto, K., de Gouw, J., Onasch, T. B., Warneke,  
336 C., and Kroll, J. H.: Biomass-burning-derived particles from a wide variety of fuels – Part 2: Effects of  
337 photochemical aging on particle optical and chemical properties, *Atmos. Chem. Phys.*, 20, 8511-8532,  
338 doi:10.5194/acp-20-8511-2020, 2020.
- 339 Chand, D., Wood, R., Anderson, T. L., Satheesh, S. K., and Charlson, R. J.: Satellite-derived direct radiative effect of  
340 aerosols dependent on cloud cover, *Nat. Geosci.*, 2, 181-184, doi:10.1038/Ngeo437, 2009.
- 341 China, S., Mazzoleni, C., Gorkowski, K., Aiken, A. C., and Dubey, M. K.: Morphology and mixing state of individual  
342 freshly emitted wildfire carbonaceous particles, *Nat. Commun.*, 4:2122 doi: 10.1038/ncomms3122, 2013.
- 343 Costantino, L., and Bréon F. M.: Aerosol indirect effect on warm clouds over South-East Atlantic from co-located  
344 MODIS and CALIPSO observations, *Atmos. Chem. Phys.*, 13, 69-88, doi:10.5194/acp-13-69-2013, 2013.
- 345 Das, S., Harshvardhan, H., and Colarco, P. R.: The influence of elevated smoke layers on stratocumulus clouds over  
346 the SE Atlantic in the NASA Goddard Earth Observing System (GEOS) Model, *J. Geophys. Res. Atmos.*, 125,  
347 e2019JD031209. doi:10.1029/2019JD031209, 2020.
- 348 Diamond, M. S., Dobracki, A., Freitag, S., Small Griswold, J. D., Heikkila, A., Howell, S. G., Kacarab, M. E.,  
349 Podolske, J. R., Saide, P. E., and Wood, R.: Time-dependent entrainment of smoke presents an observational  
350 challenge for assessing aerosol–cloud interactions over the southeast Atlantic Ocean, *Atmos. Chem. Phys.*, 18,  
351 14623–14636, <https://doi.org/10.5194/acp-18-14623-2018>, 2018.
- 352 Doherty, S. J., Saide, P. E., Zuidema, P., Shinzuka, Y., Ferrada, G. A., Gordon, H., Mallet, M., Meyer, K.,  
353 Painemal, D., Howell, S. G., Freitag, S., Dobracki, A., Podolske, J. R., Burton, S. P., Ferrare, R. A., Howes, C.,  
354 Nabat, P., Carmichael, G. R., da Silva, A., Pistone, K., Chang, I., Gao, L., Wood, R., and Redemann, J.: Modeled  
355 and observed properties related to the direct aerosol radiative effect of biomass burning aerosol over the Southeast  
356 Atlantic, *Atmos. Chem. Phys.*, 22, 1-46, <https://doi.org/10.5194/acp-22-1-2022>, 2022.
- 357 Gordon, H., Field, P. R., Abe, S. J., Dalvi, M., Grosvenor, D. P., Hill, A. A., Johnson, B. T., Miltenberger, A. K.,  
358 Yoshioka, M., and Carslaw, K. S.: Large simulated radiative effects of smoke in the south-east Atlantic, *Atmos.*  
359 *Chem. Phys.*, 18, 15261-15289, doi:10.5194/acp-18-15261-2018, 2018.
- 360 Grund, C. J., and Eloranta, E. W.: University of Wisconsin high spectral resolution lidar, *Opt. Eng.*, 30, 6-12, 1991.
- 361 Gupta, S., McFarquhar, G. M., O'Brien, J. R., Poellot, M. R., Delene, D. J., Miller, R. M., and Small Griswold, J. D.:  
362 Precipitation Susceptibility of Marine Stratocumulus with Variable Above and Below-Cloud Aerosol  
363 Concentrations over the Southeast Atlantic, *Atmos. Chem. Phys. Discuss.* [preprint], [https://doi.org/10.5194/acp-](https://doi.org/10.5194/acp-2021-677)  
364 [2021-677](https://doi.org/10.5194/acp-2021-677), in review, 2021.
- 365 Hair, J. W., Hostetler, C. A., Cook, A. L., Harper, D. B., Ferrare, R. A., Mack, T. L., Welch, W., Izquierdo, L. R.,  
366 Hovis, F. E.: Airborne High Spectral Resolution Lidar for profiling aerosol optical properties, *Appl. Optics*, 47, doi:  
367 10.1364/AO.47.006734, 2008.

368 Haywood, J. M., Osborne, S. R., Francis, P. N., Keil, A., Formenti, P., Andreae, M. O., and Kaye, P. H.: The mean  
 369 physical and optical properties of regional haze dominated by biomass burning aerosol measured from the C-130  
 370 aircraft during SAFARI 2000, *J. Geophys. Res.*, 108, 8473, <https://doi.org/10.1029/2002JD002226>, 2003.  
 371 Haywood, J. M., Abel, S. J., Barrett, P. A., Bellouin, N., Blyth, A., Bower, K. N., Brooks, M., Carslaw, K., Che, H.,  
 372 Coe, H., Cotterell, M. I., Crawford, I., Cui, Z., Davies, N., Dingley, B., Field, P., Formenti, P., Gordon, H., de  
 373 Graaf, M., Herbert, R., Johnson, B., Jones, A. C., Langridge, J. M., Malavelle, F., Partridge, D. G., Peers, F.,  
 374 Redemann, J., Stier, P., Szpek, K., Taylor, J. W., Watson-Parris, D., Wood, R., Wu, H., and Zuidema, P.: The  
 375 CLOUD–Aerosol–Radiation Interaction and Forcing: Year 2017 (CLARIFY-2017) measurement campaign, *Atmos.*  
 376 *Chem. Phys.*, 21, 1049–1084, <https://doi.org/10.5194/acp-21-1049-2021>, 2021.  
 377 Kacarab, M., Thornhill, K. L., Dobracki, A., Howell, S. G., O'Brien, J. R., Freitag, S., Poellot, M. R., Wood, R.,  
 378 Zuidema, P., Redemann, J., and Nenes, A.: Biomass burning aerosol as a modulator of the droplet number in the  
 379 southeast Atlantic region, *Atmos. Chem. Phys.*, 20, 3029–3040, <https://doi.org/10.5194/acp-20-3029-2020>, 2020.  
 380 Keil, A., and Haywood, J. M.: Solar radiative forcing by biomass burning aerosol particles during SAFARI 2000: A  
 381 case study based on measured aerosol and cloud properties, *J. Geophys. Res. Atmos.*, 108, 8467,  
 382 doi:10.1029/2002JD002315, 2003.  
 383 Klopper, D., Formenti, P., Namwoonde, A., Cazaunau, M., Chevaillier, S., Feron, A., Gaimoz, C., Hease, P., Lahmidi,  
 384 F., Mirande-Bret, C., Triquet, S., Zeng, Z., and Piketh, S. J.: Chemical composition and source apportionment of  
 385 atmospheric aerosols on the Namibian coast, *Atmos. Chem. Phys.*, 20, 15,811–15,833, doi:10.5194/acp-20-15811-  
 386 2020, 2020.  
 387 Koch, D., and Del Genio A. D.: Black carbon semi-direct effects on cloud cover: review and synthesis, *Atmos. Chem.*  
 388 *Phys.*, 10, 7685–7696, doi:10.5194/acp-10-7685-2010, 2010.  
 389 Lu, Z., Liu, X., Zhang, Z., Zhao, C., Meyer, K., Rajapakshe, C., Wu, C., Yang, Z., and Penner, J.: Biomass smoke  
 390 from southern Africa can significantly enhance the brightness of stratocumulus over the southeastern Atlantic  
 391 Ocean, *Proc. Natl. Acad. Sci.*, 115, 2924–2929, doi:10.1073/pnas.1713703115, 2018.  
 392 Mallet, M., Solmon, F., Nabat, P., Elguindi, N., Waquet, F., Bouniol, D., Sayer, A. M., Meyer, K., Roehrig, R.,  
 393 Michou, M., Zuidema, P., Flaant, C., Redemann, J., and Formenti, P.: Direct and semi-direct radiative forcing of  
 394 biomass-burning aerosols over the southeast Atlantic (SEA) and its sensitivity to absorbing properties: a regional  
 395 climate modeling study, *Atmos. Chem. Phys.*, 20, 13191–13216, <https://doi.org/10.5194/acp-20-13191-2020>, 2020.  
 396 McFarquhar, G. M., and Wang, H.: Effects of aerosols on trade wind cumuli over the Indian Ocean: Model  
 397 simulations, *Q. J. R. Meteorol. Soc.*, 132, 821–843, doi: 10.1256/qj.04.179, 2006.  
 398 Mechoso, C. R., Wood, R., Weller, R., Bretherton, C. S., Clarke, A. D., Coe, H., Fairall, C., Farrar, J. T., Feingold,  
 399 G., Garreaud, R., Grados, C., McWilliams, J., de Szoeke, S. P., Yuter, S. E., and Zuidema, Z.: Ocean–cloud–  
 400 atmosphere–land interactions in the Southeastern Pacific: The VOCALS program, *B. Am. Meteorol. Soc.*, 95, 357-  
 401 375, doi:10.1175/BAMS-D-11-00246.1, 2013.  
 402 Meyer, K., Platnick, S., Oreopoulos, L., and Lee, D.: Estimating the direct radiative effect of absorbing aerosols  
 403 overlying marine boundary layer clouds in the southeast Atlantic using MODIS and CALIOP, *J. Geophys. Res.*  
 404 *Atmos.*, 118, 4801–4815, doi:10.1002/jgrd.50449, 2013.  
 405 Müller, D., Wandinger, U., and Ansmann, A.: Microphysical particle parameters from extinction and backscatter lidar  
 406 data by inversion with regularization: theory, *Appl. Optics*, 38, 2346–2357, 1999a.  
 407 Müller, D., Wandinger, U., and Ansmann, A.: Microphysical particle parameters from extinction and backscatter lidar  
 408 data by inversion with regularization: simulation, *Appl. Optics*, 38, 2358–2368, 1999b.  
 409 Müller, D., Hostetler, C. A., Ferrare, R. A., Burton, S. P., Chemyakin, E., Kolgotin, A., Hair, J. W., Cook, A. L.,  
 410 Harper, D. B., Rogers, R. R., Hare, R. W., Cleckner, C. S., Obland, M. D., Tomlinson, J., Berg, L. K., and Schmid,  
 411 B.: Airborne multiwavelength high spectral resolution lidar (HSRL-2) observations during TCAP 2012: vertical  
 412 profiles of optical and microphysical properties of a smoke/urban haze plume over the northeastern coast of the US,  
 413 *Atmos. Meas. Tech.*, 7, 3487–3496, doi:10.5194/amt-7-3487-2014, 2014.  
 414 Müller, D., Chemyakin, E., Kolgotin, A., Ferrare, R. A., Hostetler, C. A., and Romanov, A.: Automated, unsupervised,  
 415 inversion of multiwavelength lidar data with TiARA: assessment of retrieval performance of microphysical  
 416 parameters using simulated data, *Appl. Optics*, 58, 4981–5007, doi:10.1364/AO.58.004981, 2019.  
 417 Painemal, D., Kato, S., and Minnis, P.: Boundary layer regulation in the southeast Atlantic cloud microphysics during  
 418 the biomass burning season as seen by the A-train satellite constellation, *J. Geophys. Res. Atmospheres*, 119,  
 419 11,288–211,302, doi:10.1002/2014JD022182, 2014.  
 420 Peers, F., Francis, P., Fox, C., Abel, S. J., Szpek, K., Cotterell, M. I., Davies, N. W., Langridge, J. M., Meyer, K. G.,  
 421 Platnick, S. E., and Haywood, J. M.: Observation of absorbing aerosols above clouds over the south-east Atlantic  
 422 Ocean from the geostationary satellite SEVIRI – Part 1: Method description and sensitivity, *Atmos. Chem. Phys.*,  
 423 19, 9595–9611, <https://doi.org/10.5194/acp-19-9595-2019>, 2019.

424 Penner, J. E., Zhang, S. Y., and Chuang, C. C.: Soot and smoke aerosol may not warm climate, *J. Geophys. Res.*  
425 *Atmospheres*, 108, 4657, doi:10.1029/2003JD003409, 2003.

426 Pistone, K., Zuidema, P., Wood, R., Diamind, M., da Silva, A. M., Ferrada, G., Saide, P. E., Ueyama, R., Ryoo, J.-  
427 M., Pfister, L., Podolske, J., Noone, D., Bennett, R., Stith, E., Carmichael, G., Redemann, J., Flynn, C., LeBlanc,  
428 S., Segal-Rozenhaimer, M., and Shinozuka, Y.: Exploring the elevated water vapor signal associated with the free  
429 tropospheric biomass burning plume over the southeast Atlantic Ocean, *Atmos. Chem. Phys.*, 21, 9643-9668,  
430 <https://doi.org/10.5194/acp-21-9643-2021>, 2021.

431 Pósfai, M., Simonics, R., Li, J., Hobbs, P. V., and Buseck, P. R.: Individual aerosol particles from biomass burning in  
432 southern Africa: 1. Compositions and size distributions of carbonaceous particles, *J. Geophys. Res.*, 108, 8483,  
433 doi:10.1029/2002JD002291, 2003.

434 Ramanathan, V., Crutzen, P. J., Kiehl, J. T., and Rosenfeld, D.: Aerosols, climate, and the hydrological cycle, *Science*,  
435 294(5549), 2119-2124, doi:10.1126/science.1064034, 2001.

436 Randles, C.A., daSilva, A. M., Buchard, V., Colarco, P. R., Darmenov, A., Govindaraju, P., Smirnov, A., Holben, B.,  
437 Ferrare, R. A., Hair, J., Shinozuka, Y., and Flynn, C. J.: The MERRA-2 aerosol reanalysis, 1980 onward. Part I:  
438 System description and data assimilation evaluation, *J. Climate*, 30, 6823–6850, doi: 10.1175/JCLI-D-16-0609.1,  
439 2017.

440 Redemann, J., Wood, R., Zuidema, P., Doherty, S. J., Luna, B., LeBlanc, S. E., Diamond, M. S., Shinozuka, Y., Chang,  
441 I. Y., Ueyama, R., Pfister, L., Ryoo, J.-M., Dobracki, A. N., da Silva, A. M., Longo, K. M., Kacenelenbogen, M.  
442 S., Flynn, C. J., Pistone, K., Knox, N. M., Piketh, S. J., Haywood, J. M., Formenti, P., Mallet, M., Stier, P.,  
443 Ackerman, A. S., Bauer, S. E., Fridlind, A. M., Carmichael, G. R., Saide, P. E., Ferrada, G. A., Howell, S. G.,  
444 Freitag, S., Cairns, B., Holben, B. N., Knobelspiesse, K. D., Tanelli, S., L'Ecuyer, T. S., Dzambo, A. M., Sy, O. O.,  
445 McFarquhar, G. M., Poellot, M. R., Gupta, S., O'Brien, J. R., Nenes, A., Kacarab, M., Wong, J. P. S., Small-  
446 Griswold, J. D., Thornhill, K. L., Noone, D., Podolske, J. R., Schmidt, K. S., Pilewskie, P., Chen, H., Cochrane, S.  
447 P., Sedlacek, A. J., Lang, T. J., Stith, E., Segal-Rozenhaimer, M., Ferrare, R. A., Burton, S. P., Hostetler, C. A.,  
448 Diner, D. J., Seidel, F. C., Platnick, S. E., Myers, J. S., Meyer, K. G., Spangenberg, D. A., Maring, H., and Guo, L.:  
449 An overview of the ORACLES (ObseRvations of Aerosols above Clouds and their intEractionS) project: aerosol-  
450 cloud-radiation interactions in the southeast Atlantic basin, *Atmos. Chem. Phys.*, 21, 1507-1563, doi:10.5194/acp-  
451 21-1507-2021, 2021.

452 Rogers, R. R., Hair, J. W., Hostetler, C. A., Ferrare, R. A., Obland, M. D., Cook, A. L., Harper, D. B., Burton, S. P.,  
453 Shinozuka, Y., McNaughton, C. S., Clarke, A. D., Redemann, J., Russell, P. B., Livingston, J. M., and Kleinman,  
454 L. I.: NASA LaRC airborne high spectral resolution lidar aerosol measurements during MILAGRO: observations  
455 and validation, *Atmos. Chem. Phys.*, 9, 4811-4826, 2009.

456 Ryoo, J.-M., Pfister, L., Ueyama, R., Zuidema, P., Wood, R., Chang, I., and Redemann, J.: A meteorological  
457 overview of the ORACLES (ObseRvations of Aerosols above CLouds and their intEractionS) campaign over the  
458 southeastern Atlantic during 2016–2018: Part 1 – Climatology, *Atmos. Chem. Phys.*, 21, 16689–16707,  
459 <https://doi.org/10.5194/acp-21-16689-2021>, 2021.

460 Sakaeda, N., Wood, R., and Rasch, P. J.: Direct and semidirect aerosol effects of southern African biomass burning  
461 aerosol, *J. Geophys. Res. Atmospheres*, 116, D12205, doi:10.1029/2010JD015540, 2011.

462 Sawamura, P., Moore, R. H., Burton, S. P., Chemyakin, E., Müller, D., Kolgotin, A., Ferrare, R. A., Hostetler, C. A.,  
463 Ziemba, L. D., Beyersdorf, A. J., and Anderson, B. E.: HSRL-2 aerosol optical measurements and microphysical  
464 retrievals vs. airborne in situ measurements during DISCOVER-AQ 2013: an intercomparison study, *Atmos. Chem.*  
465 *Phys.*, 17, 7229-7243, doi.org/10.5194/acp-17-7229-2017, 2017.

466 Schmid, B., Ferrare, R. A., Flynn, C., Elleman, R., Covert, D., Strawa, A., Welton, E., Turner, D., Jonsson, H.,  
467 Redemann, J., Eilers, J., Ricci, K., Hallar, A. G., Clayton, M., Michalsky, J., Smirnov, A., Holben, B., and Barnard,  
468 J. : How well do state-of-the-art techniques measuring the vertical profile of tropospheric aerosol extinction  
469 compare? *J. Geophys. Res.*, 111, D05S07, doi:10.1029/2005JD005837, 2006.

470 She, C. Y., Alvarez II, R. J., Caldwell, L. M., and Krueger, D. A.: High-spectral-resolution Rayleigh-Mie lidar  
471 measurement of aerosol and atmospheric profiles, *Opt. Lett.*, 17, 541-543, 1992.

472 Shingler, T., Crosbie, E., Ortega, A., Shiraiwa, M., Zuend, A., Beyersdorf, A., Ziemba, L., Anderson, B., Thornhill,  
473 L., Perring, A. E., Schwarz, J. P., Campazano-Jost, P., Day, D. A., Jimenez, J. L., Hair, J. W., Mikoviny, T.,  
474 Wisthaler, A., & Sorooshian, A.: Airborne characterization of subsaturated aerosol hygroscopicity and dry refractive  
475 index from the surface to 6.5km during the SEAC<sup>4</sup>RS campaign, *J. Geophys. Res.*, 121(8), 4188-4210,  
476 <https://doi.org/10.1002/2015JD024498>, 2016.

477 Shinozuka, Y., Saide, P. E., Ferrada, G. A., Burton, S. P., Ferrare, R. A., Doherty, S. J., Gordon, H., Longo, K., Mallet,  
478 M., Feng, Y., Wang, Q., Cheng, Y., Dobracki, A., Freitag, S., Howell, S. G., LeBlanc, S., Flynn, C., Segal-  
479 Rozenhaimer, M., Pistone, K., Podolske, J. R., Stith, E. J., Bennett, J. R., Carmichael, G. R., da Silva, A.,

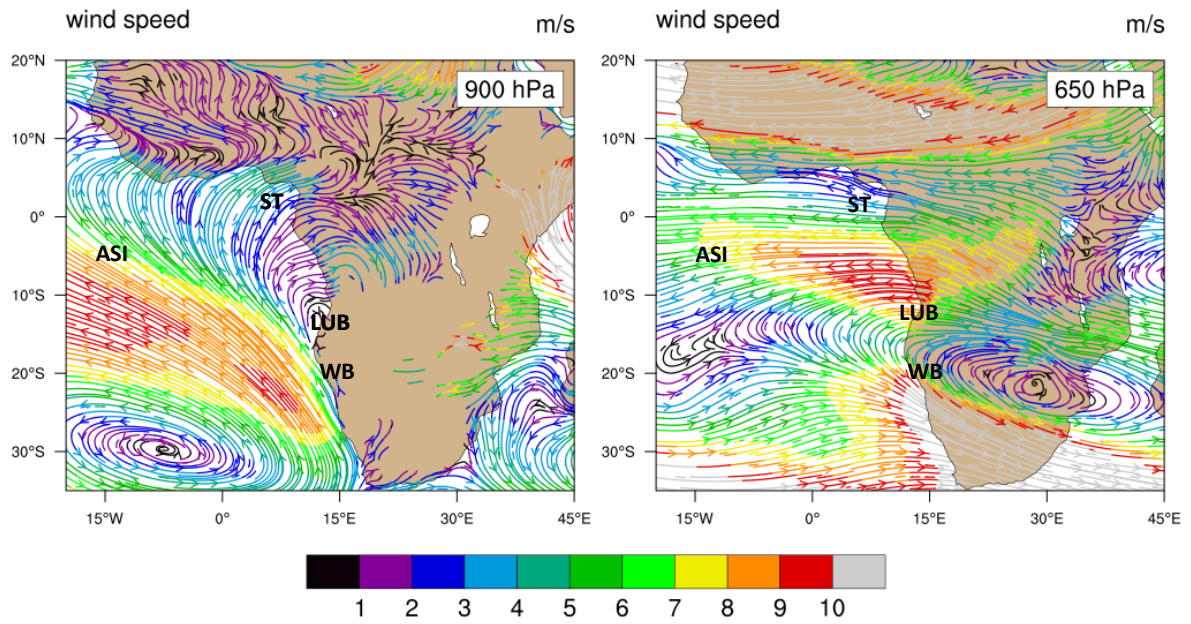
480 Govindaraju, R., Leung, R., Zhang, Y., Pfister, L., Ryoo, J.-M., Redemann, J., Wood, R., and Zuidema, P.: Modeling  
 481 of the smoky troposphere of the southeast Atlantic: a comparison to ORACLES airborne observations from  
 482 September of 2016, *Atmos. Chem. Phys.*, 20, 11491-11526, doi:10.5194/acp-20-11491-2020, 2020.  
 483 Shipley, S. T., Tracy, D. H., Eloranta, E. W., Tauger, J. T., Stroga, J. T., Roesler, F. L., and Weinman, J. A.: High  
 484 spectral resolution lidar to measure optical scattering properties of atmospheric aerosols. 1. Theory and  
 485 instrumentation, *Appl. Optics*, 22, 3716-3724, 1983.  
 486 Stein, A.F., Draxler, R. R., Rolph, G. D., Stunder, B. J. B., Cohen, M. D., and Ngan, F.: NOAA's HYSPLIT  
 487 atmospheric transport and dispersion modeling system, *B. Am. Meteorol. Soc.*, 96, 2059-2077, doi:10.1175/BAMS-  
 488 D-14-00110.1, 2015.  
 489 Veselovskii, I., Kolgotin, A., Grazianov, V., Müller, D., Wandinger, U., and Whiteman, D. N.: Inversion with  
 490 regularization for the retrieval of tropospheric aerosol parameters from multi-wavelength lidar sounding, *Appl.*  
 491 *Optics*, 41, 3685-3699, 2002.  
 492 Wilcox, E. M.: Stratocumulus cloud thickening beneath layers of absorbing smoke aerosol, *Atmos. Chem. Phys.*, 10,  
 493 11769-11777, doi:10.5194/acp-10-11769-2010, 2010.  
 494 Wilcox, E. M.: Direct and semi-direct radiative forcing of smoke aerosols over clouds, *Atmos. Chem. Phys.*, 12, 139-  
 495 149, doi:10.5194/acp-12-139-2012, 2012.  
 496 Wu, H., Taylor, J. W., Szpek, K., Langridge, J. M., Williams, P. I., Flynn, M., Allan, J. D., Abel, S. J., Pitt, J., Cotterell,  
 497 M. I., Fox, C., Davies, N. W., Haywood, J., and Coe, H.: Vertical variability of the properties of highly aged biomass  
 498 burning aerosol transported over the southeast Atlantic during CLARIFY-2017, *Atmos. Chem. Phys.*, 20, 12697-  
 499 12719, <https://doi.org/10.5194/acp-20-12697-2020>, 2021.  
 500 Xu F., Gao, L., Redemann, J., Flynn C.J., Espinosa, W.R., da Silva, A.M., Starnes, S., Burton, S.P., Liu, X., Ferrare,  
 501 R., Cairns, B. and Dubovik, O.: A Combined Lidar-Polarimeter Inversion Approach for Aerosol Remote Sensing  
 502 Over Ocean, *Front. Remote Sens*, 2:620871, doi: 10.3389/frsen.2021.620871, 2021.  
 503 Yamaguchi T, Feingold, G., Kazil, J., and McComiskey, A.: Stratocumulus to cumulus transition in the presence of  
 504 elevated smoke layers. *Geophys. Res. Lett.*, 42: 10478–10485, 2015.  
 505 Zhang, J. and Zuidema, P.: The diurnal cycle of the smoky marine boundary layer observed during August in the  
 506 remote southeast Atlantic, *Atmos. Chem. Phys.*, 19, 14493–14516, <https://doi.org/10.5194/acp-19-14493-2019>,  
 507 2019.  
 508 Zhang Z., Meyer, K., Yu, H., Platnick, S., Colarco, P. R., Liu, Z., and Oreopoulos, L.: Shortwave direct radiative  
 509 effects of above-cloud aerosols over global oceans derived from 8 years of CALIPSO and MODIS observations,  
 510 *Atmos. Chem. Phys.*, 16, 2877-2900, doi:10.5194/acp-16-2877-2016, 2016.  
 511 Zhang, X., Mao, M., Yin, Y., and Tang, S.: The absorption Ångström exponent of black carbon with brown coatings:  
 512 effects of aerosol microphysics and parameterization, *Atmos. Chem. Phys.*, 20, 9701-9711, doi:10.5194/acp-20-  
 513 9701-2020, 2020.  
 514 Zuidema, P., Redemann, J., Haywood, J., Wood, R., Piketh, S., Hipondoka, M., and Formenti, P.: Smoke and clouds  
 515 above the southeast Atlantic, *B. Am. Meteorol. Soc.*, 97, 1131-1135, doi:10.1175/BAMS-D-15-00082.1, 2016.  
 516 Zuidema, P., Sedlacek III, A. J. Flynn, C., Springston, S., Delgado, R., Zhang, J., Aiken, A. C., Koontz, A., and  
 517 Muradyan, P.: The Ascension Island boundary layer in the remote Southeast Atlantic is often smoky, *Geophys. Res.*  
 518 *Lett.*, 45, 4456-4465, doi:10.1002/2017/GL076926, 2018.  
 519

520  
521  
522

**Table 1:** Averaging area, flight time periods, the duration over water and number of HYSPLIT backward trajectories, and number of HSRL-2 profiles in each grid box used in the study.

<b>Box</b>	<b>Averaging Area</b>	<b>Averaging Days</b>	<b>Time of Day</b>	<b>Duration in Hours Over Water at 3.5 km</b>	<b>Number of Profiles</b>
A	11° S-9° S; 1° W-1° E	9/12,16	11:00 UTC	44.3±7.0 (N = 19)	50
B	10° S-8° S; 8° E-10° E	9/12,16,18	10:00 UTC	14.9±4.5 (N = 27)	56
C	16° S-14° S; 4° E-6° E	9/12,16	13:00 UTC	40.4±7.2 (N = 19)	51
D	14° S-12° S; 10° E-12° E	9/18,24	09:00 UTC	5.5±2.0 (N = 27)	46
E	23° S-21° S; 8° E-10° E	9/20,22	14:00 UTC	-	36

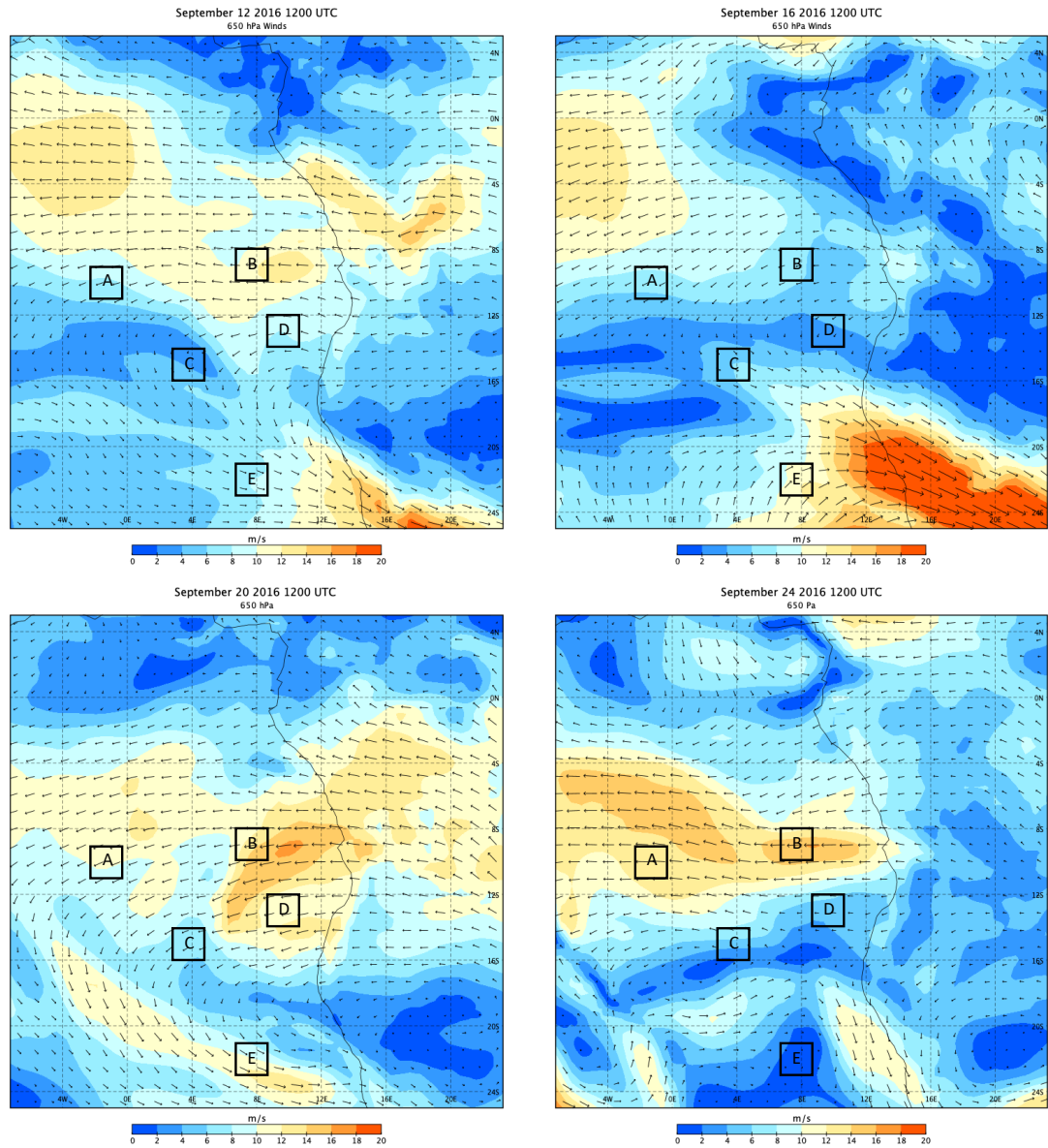
523



525  
 526  
 527  
 528  
 529  
 530

**Figure 1:** MERRA2 monthly mean reanalysis of 900 and 650 hPa streamlines for September 2016. Stations marked are Ascension Island (ASI), Lubango (LUB), a long-term AERONET site at 2 km elevation, and Walvis Bay (WB), where ER-2 flights originated from during the September 2016 ORACLES IOP. Flights in August 2017 and September/October 2018 originated from São Tomé (ST).

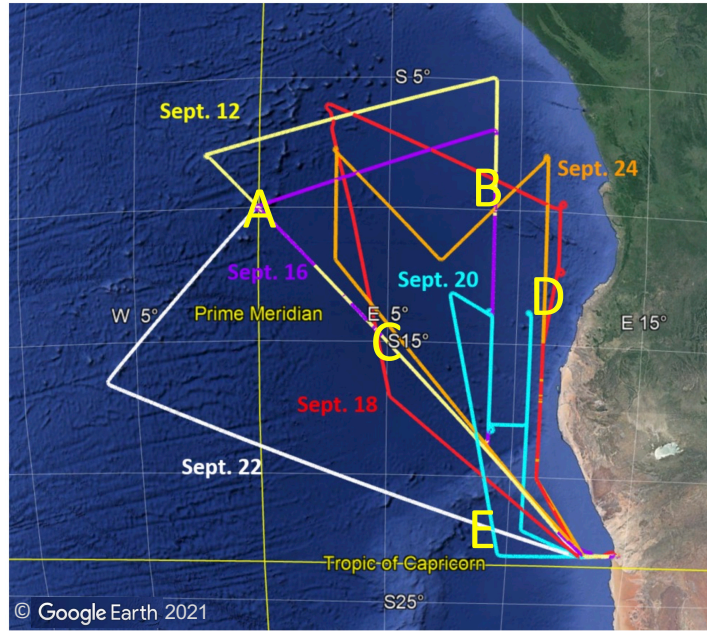




531  
532  
533  
534

**Figure 2:** MERRA2 reanalysis of 650 hPa winds at 1200 UTC on September 12, 16, 20, 24, 2016. Grid boxes in the study are marked with letters.

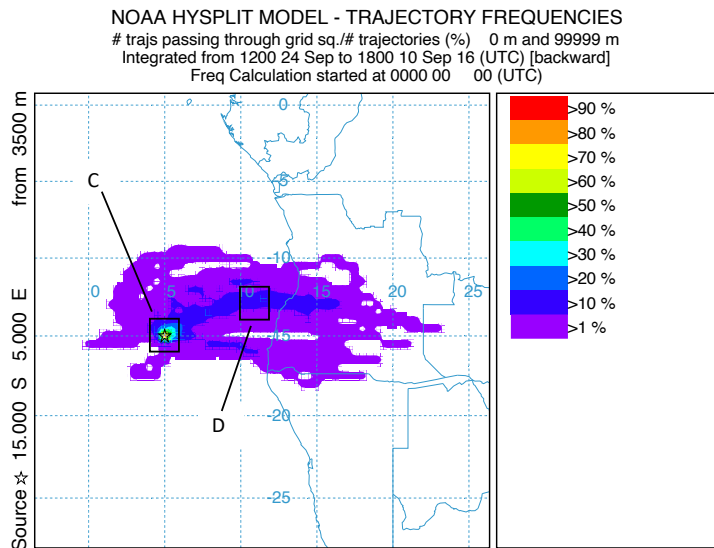
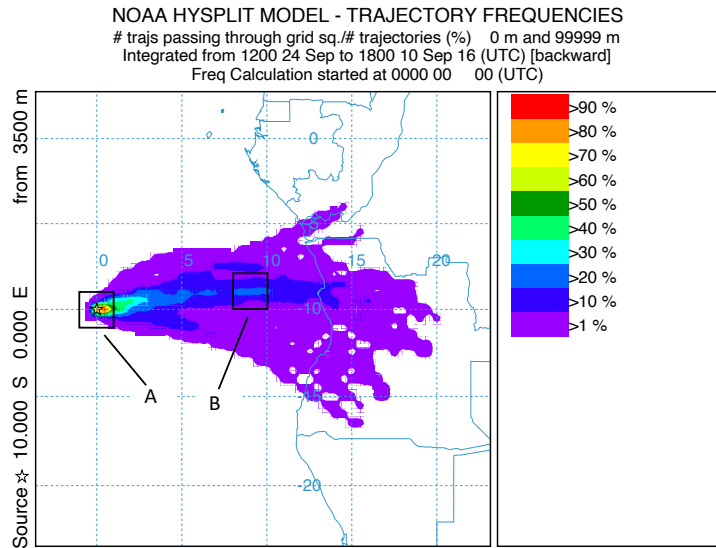
535  
536



537  
538

539  
540  
541

**Figure 3:** HSRL-2 science data flight tracks during the September 2016 IOP. Letters refer. to the grid boxes identified in Fig. 2



543  
 544  
 545  
 546  
 547  
 548

**Figure 4:** Frequency distribution of 48-hour backward trajectories of air parcels arriving at 3500 m above the centers of grid boxes A and C over the time period of the campaign. Grid boxes B and D are upstream of grid boxes A and C, respectively.

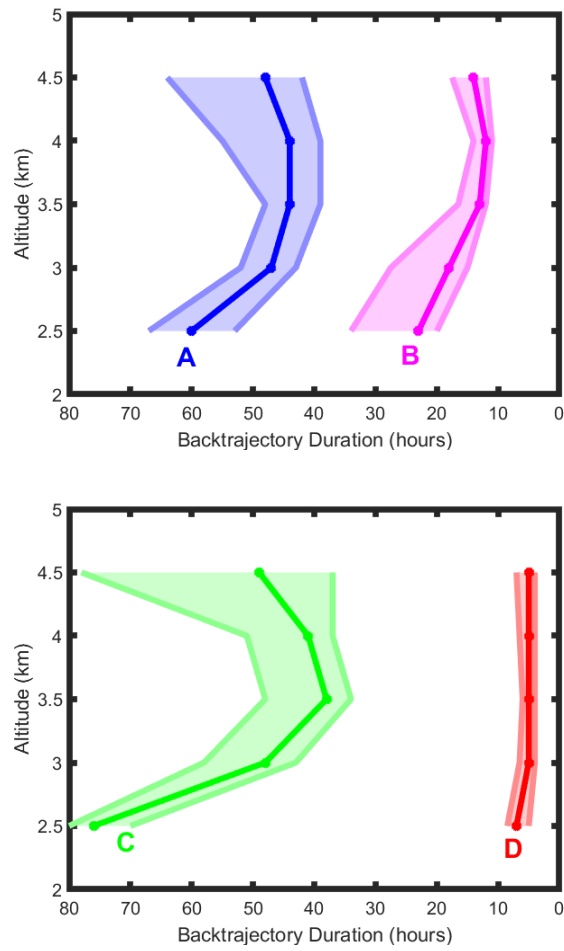
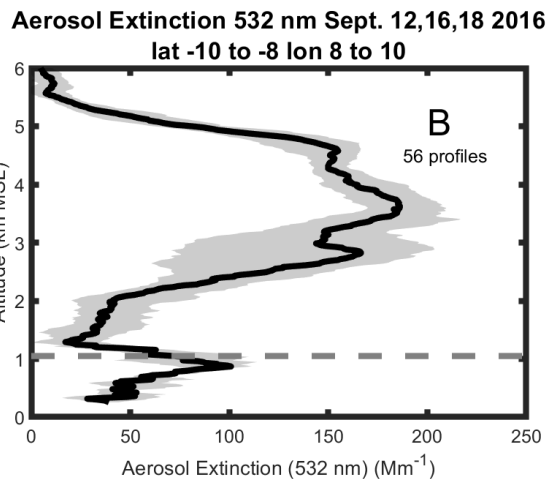
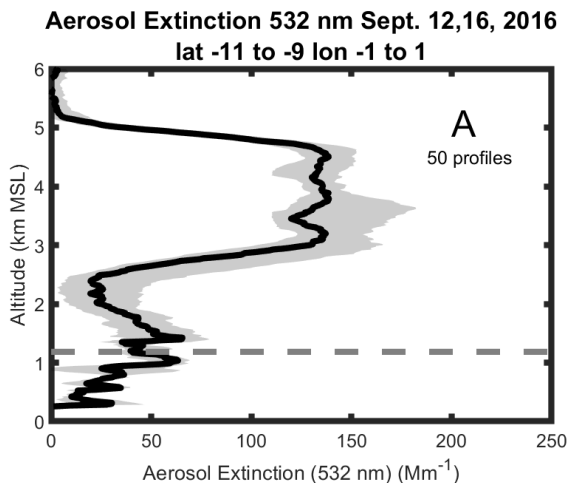


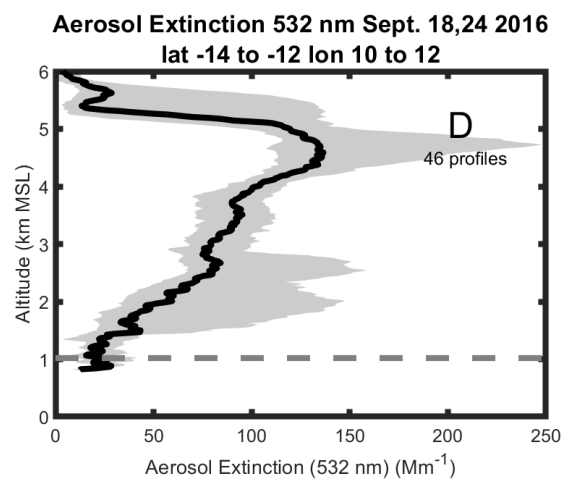
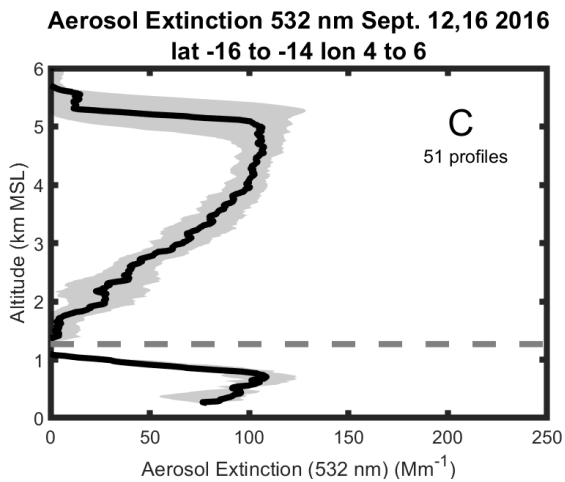
**Figure 5:** Duration of time spent over water of air parcels arriving at grid boxes marked on the figure. Solid lines are median values, and the shaded portion are the range of the 75<sup>th</sup> and 25<sup>th</sup> percentile. The number of trajectories used for the calculation are in Table 1. Trajectory hours are shown in reverse to correspond to the map in Fig. 4.

550  
 551  
 552  
 553  
 554  
 555  
 556

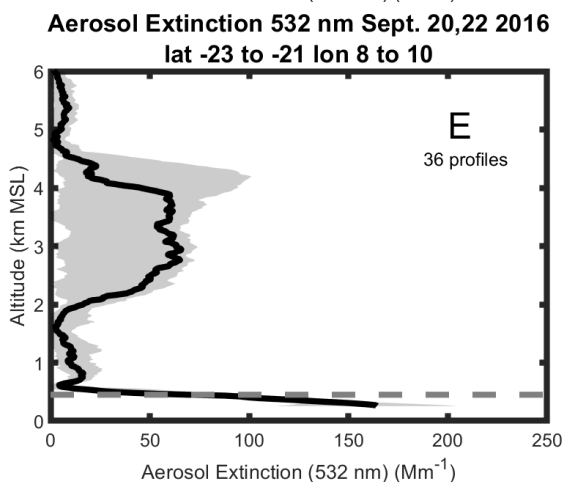
557



558



559



560

561

562

563

564

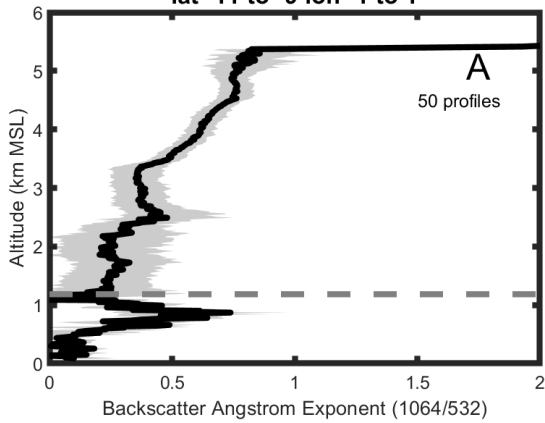
565

566

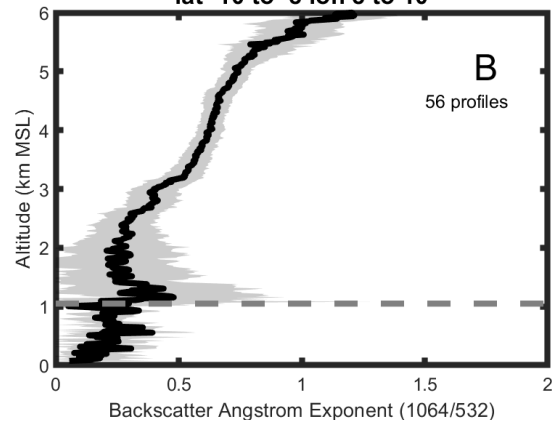
**Figure 6:** Average vertical profiles of the aerosol extinction coefficient at 532 nm in grid boxes A (upper left), B (upper right), C (middle left), D (middle right) and E (lower left). The averaging area, dates of flights and total number of one-minute profiles are also shown. The dark line represents the median value and grey shades contain the 25<sup>th</sup> to 75<sup>th</sup> percentiles. Dashed line refers to the mean cloud top height.

567

**Backscatter Ang. Expo. 1064/532 Sept. 12,16, 2016**  
**lat -11 to -9 lon -1 to 1**

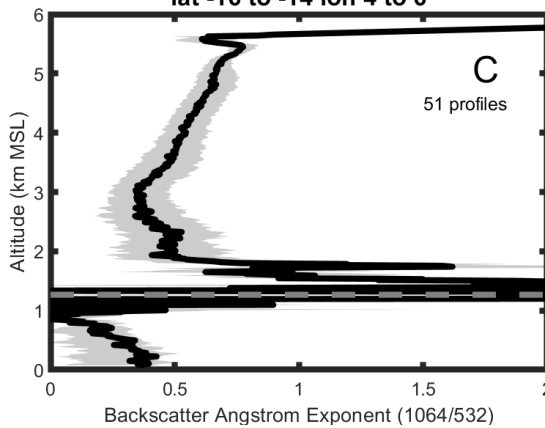


**Backscatter Ang. Expo. 1064/532 Sept. 12,16,18 2016**  
**lat -10 to -8 lon 8 to 10**

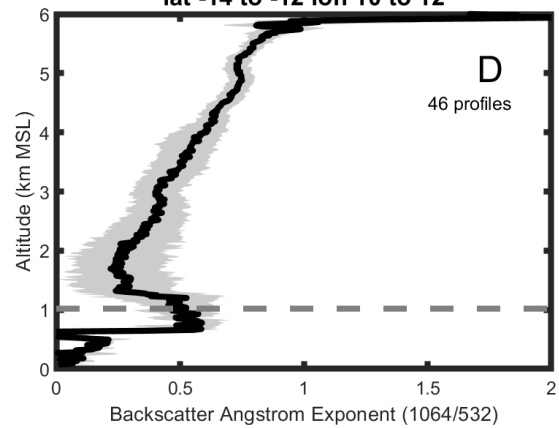


568

**Backscatter Ang. Expo. 1064/532 Sept. 12,16 2016**  
**lat -16 to -14 lon 4 to 6**

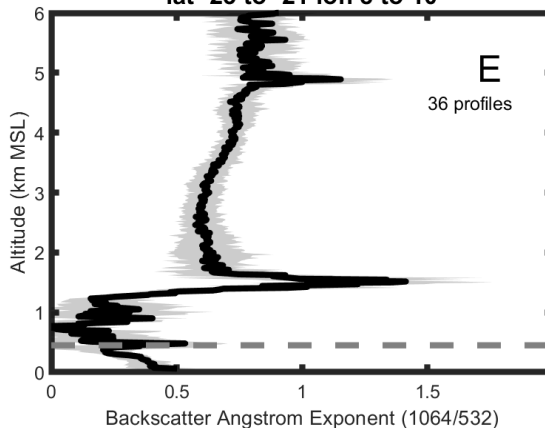


**Backscatter Ang. Expo. 1064/532 Sept. 18,24 2016**  
**lat -14 to -12 lon 10 to 12**



569

**Backscatter Ang. Expo. 1064/532 Sept. 20,22 2016**  
**lat -23 to -21 lon 8 to 10**



570

571

572

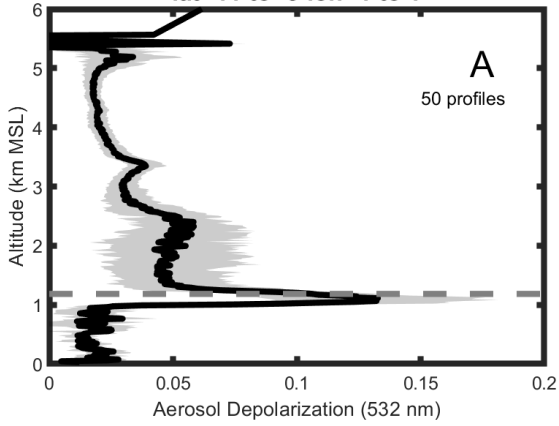
573

574

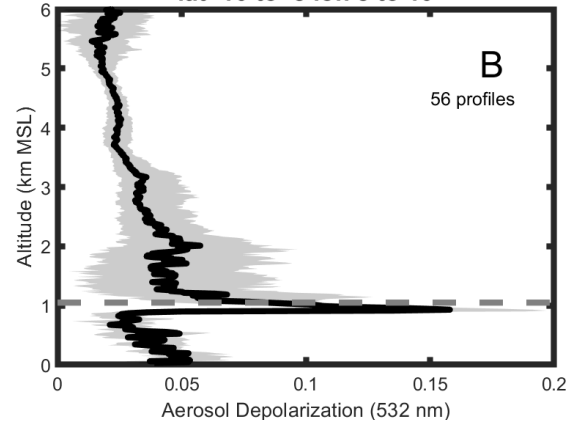
**Figure 7:** As in Fig. 6 but for the Wavelength Dependent Backscatter Ångström exponent between 1064 and 532 nm.

575

**Aerosol Depolarization 532 nm Sept. 12,16, 2016**  
lat -11 to -9 lon -1 to 1

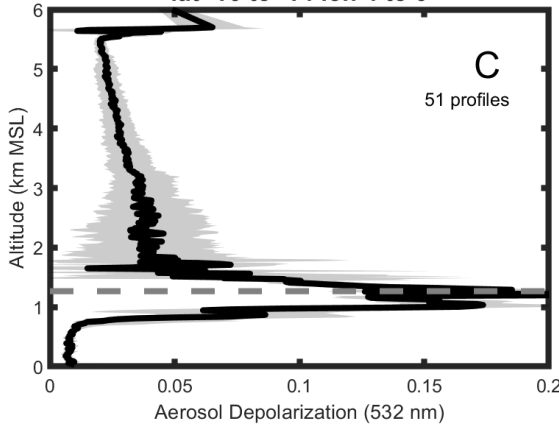


**Aerosol Depolarization 532 nm Sept. 12,16,18 2016**  
lat -10 to -8 lon 8 to 10

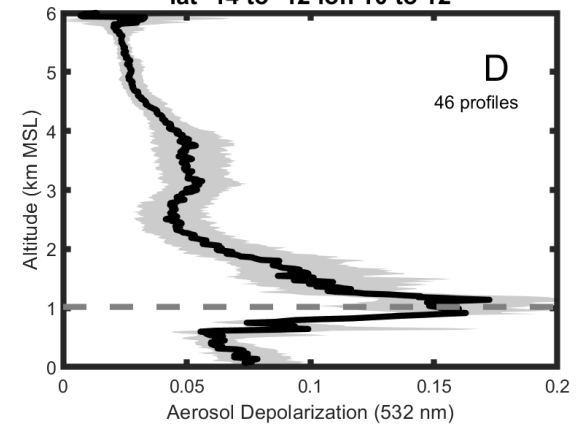


576

**Aerosol Depolarization 532 nm Sept. 12,16 2016**  
lat -16 to -14 lon 4 to 6

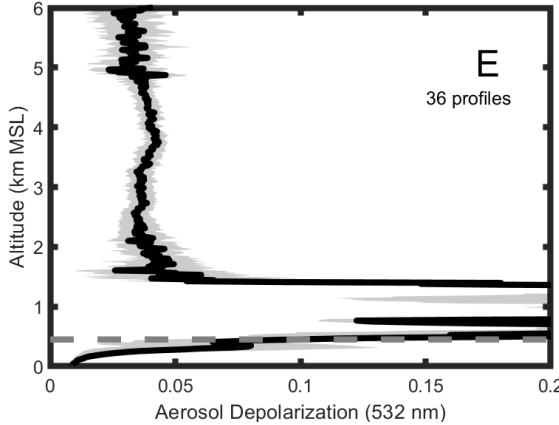


**Aerosol Depolarization 532 nm Sept. 18,24 2016**  
lat -14 to -12 lon 10 to 12



577

**Aerosol Depolarization 532 nm Sept. 20,22 2016**  
lat -23 to -21 lon 8 to 10



578

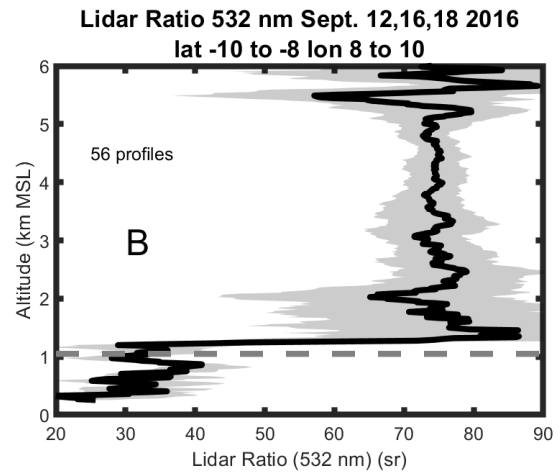
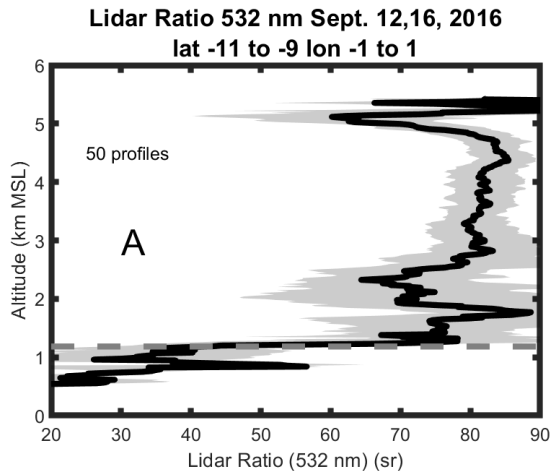
579

580

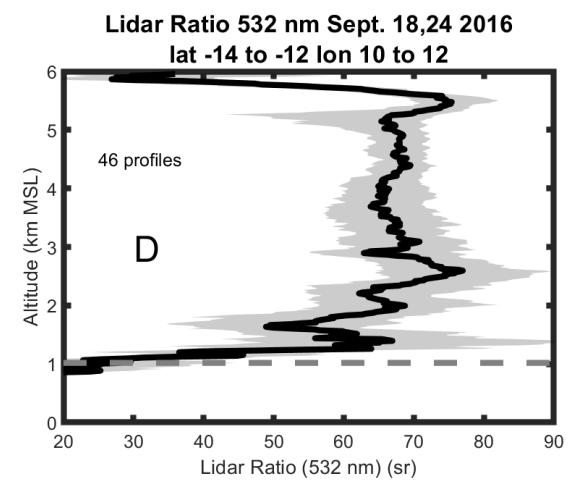
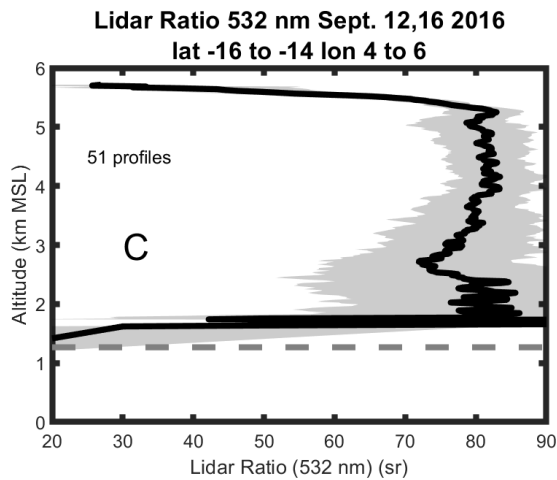
581

**Figure 8:** As in Fig. 6 but for the aerosol depolarization at 532 nm.

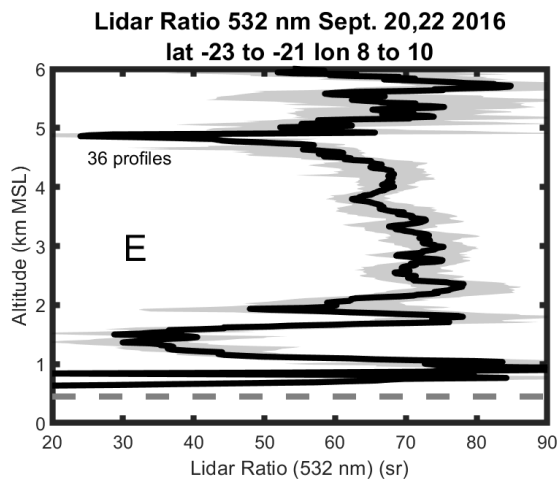
582



583



584

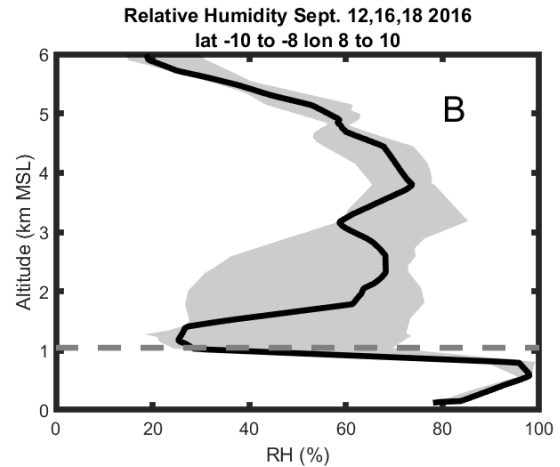
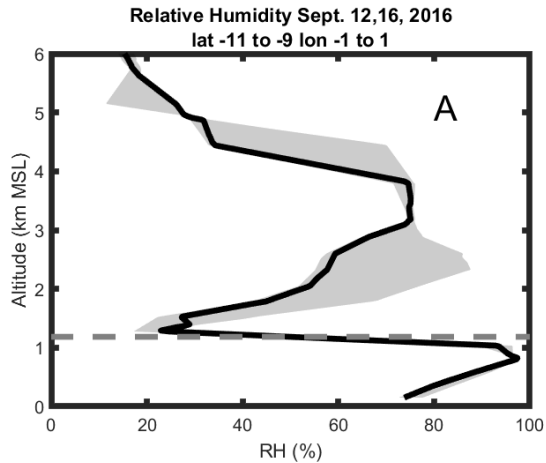


585  
586  
587  
588

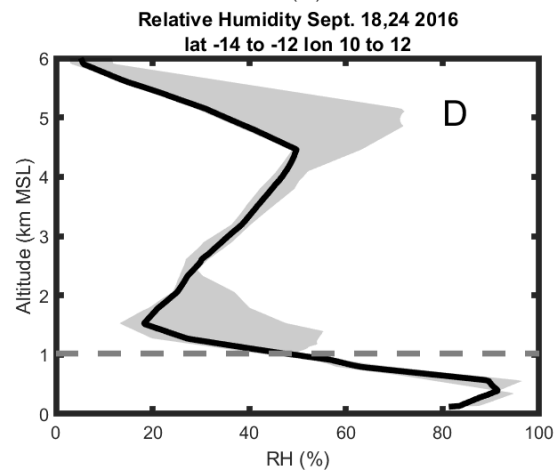
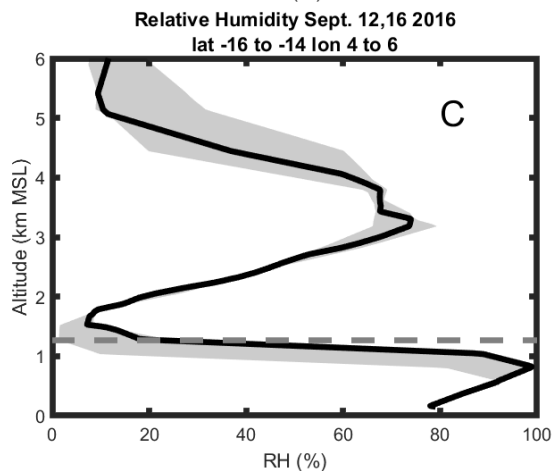
**Figure 9:** As in Fig. 6 but for the Lidar Ratio at 532 nm.



589



590



591  
592  
593  
594  
595  
596  
597  
598

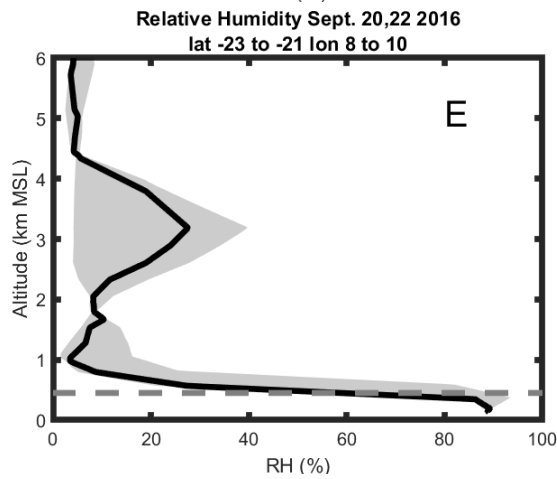
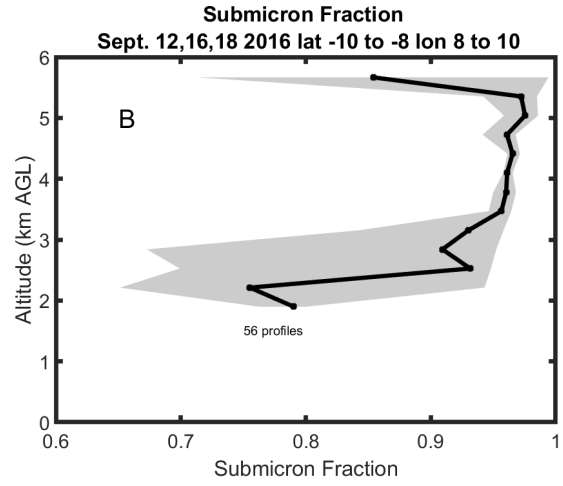
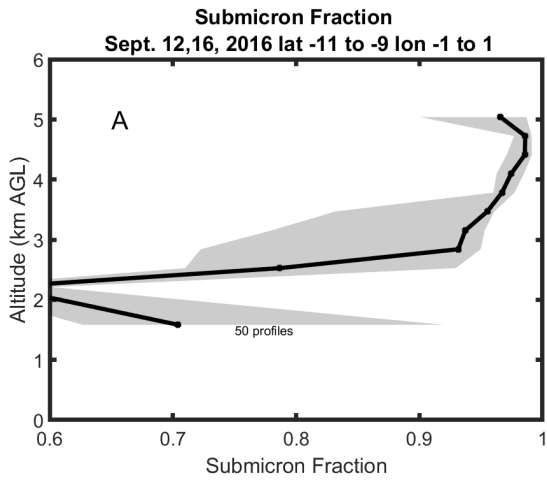
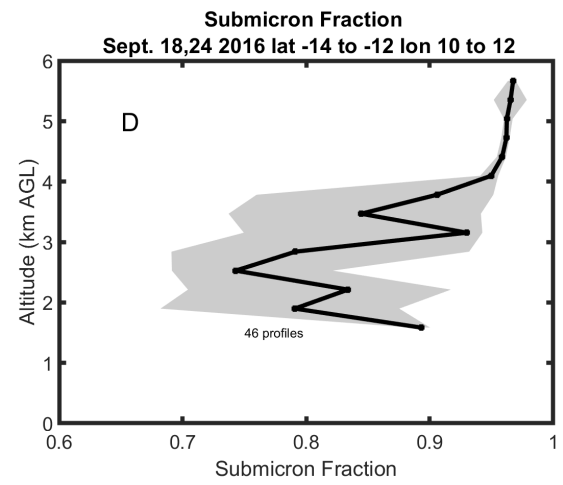
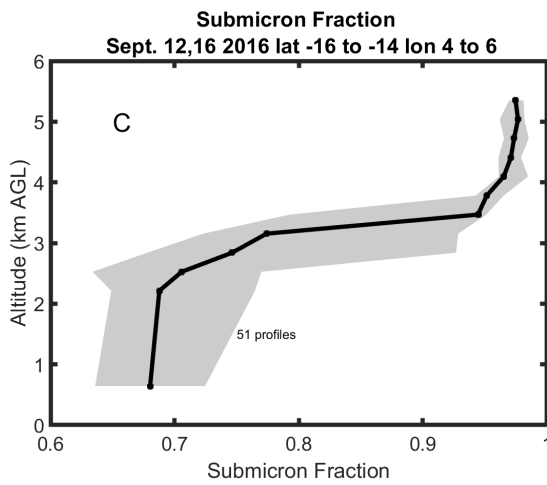


**Figure 10:** Relative Humidity (%) in grid boxes A (upper left), B (upper right), C (middle left), D (middle right) and E (lower left) from MERRA2 reanalysis corresponding to the HSRL-2 profiles shown in Figs. 6-9. The dark line represents the median value and grey shades contain the 25<sup>th</sup> to 75<sup>th</sup> percentiles. Dashed line refers to the mean cloud top height.

599



600



601  
602  
603  
604  
605  
606  
607

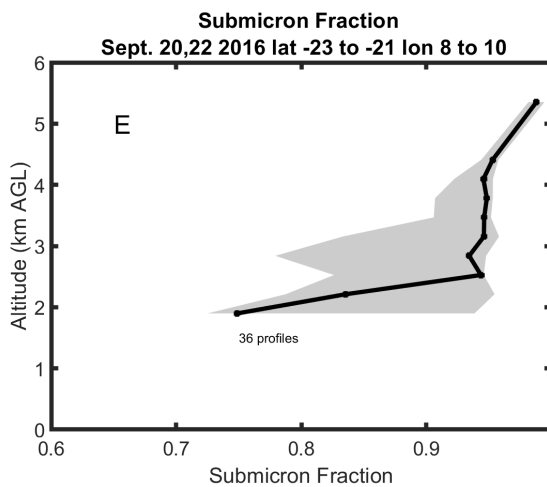
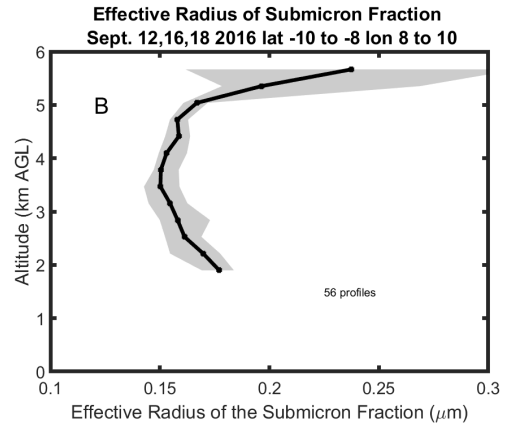
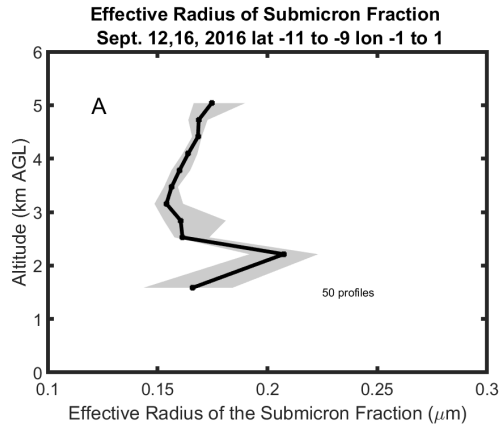
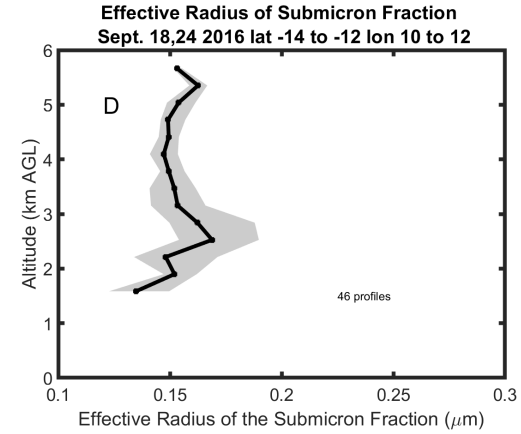
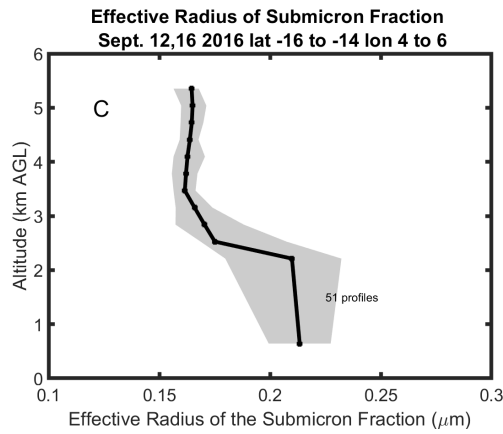


**Figure 11:** Average vertical profiles of the submicron fraction in grid boxes A (upper left), B (upper right), C (middle left), D (middle right) and E (lower left). The averaging area, dates of flights and total number of one-minute profiles in the average are also shown. The dark line represents the median value and grey shades contain the 25<sup>th</sup> to 75<sup>th</sup> percentiles.

608



609



610

611

612

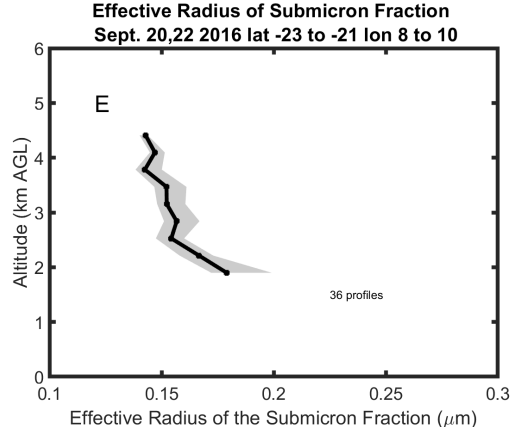


**Figure 12:** As in Fig. 11 but for the effective radius of the submicron fraction.